Post Irradiation Examination of Nanoprecipitate Stability and α' Precipitation in an Oxide Dispersion Strengthened Fe-12Cr-5Al Alloy

Caleb P. Massey[a,1], Philip D. Edmondson[b], Kevin G. Field[b], David T. Hoelzer[b], Sebastien N. Dryepondt[b], Kurt A. Terrani[b] and Steven J. Zinkle[a,b]

[a] Department of Nuclear Engineering, University of Tennessee, Knoxville, TN 37996
[b] Oak Ridge National Laboratory, Oak Ridge, TN 37831
Corresponding author: cmassey7@utk.edu

Keywords: atom probe tomography, oxide dispersion strengthened (ODS) alloy, precipitation, neutron irradiation

ABSTRACT

Oxide dispersion strengthened (ODS) FeCrAl alloy (Fe-12Cr-5Al wt.%) was neutron irradiated to 1.8 displacements per atom (dpa) at 215, 357, and 557°C to investigate (Y,Al,O) nano-oxide stability and Cr-rich α' precipitate formation using atom probe tomography. The nano-oxide sizes remain unchanged after irradiation, but the compositions are dependent on irradiation temperature due to competition between ballistic dissolution and precipitate reformation. Cr-rich clusters observed after 357°C irradiation have lower Cr contents (61 at.%) than equilibrium α', with a lower number density than wrought FeCrAl alloys. This suggests a suppression of α' precipitation due to the high sink strength of ODS FeCrAl.

Graphical Abstract

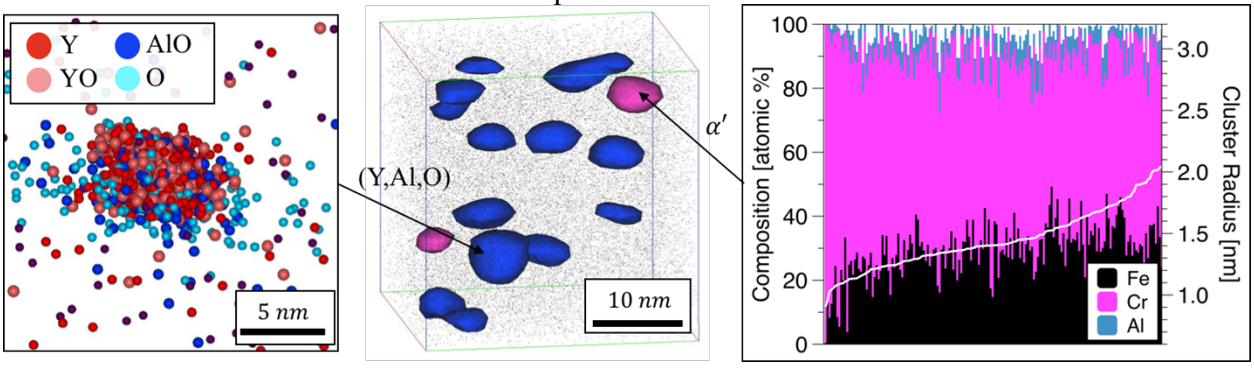

This manuscript has been authored by UT-Battelle, LLC, under Contract No. DE-AC05-00OR22725 with the U.S. Department of Energy. The United States Government retains and the publisher, by accepting the article for publication, acknowledges that the United States Government retains a non-exclusive, paid-up, irrevocable, worldwide license to publish or reproduce the published form of this manuscript, or allow others to do so, for United States Government purposes. The Department of Energy will provide public access to these results of federally sponsored research in accordance with the DOE Public Access Plan (http://energy.gov/downloads/doe-public-access-plan).

The realization of advanced fission and fusion reactor concepts will require the development of materials specifically designed to operate under high temperatures (300-1000°C) and irradiation doses (>50 displacements per atom, or dpa) [1]. Furthermore, the recent desire for materials capable of reducing the impact of nuclear accident scenarios has accelerated research into materials that can retain their high temperature strength and oxidation resistance [2]. Oxide dispersion strengthened (ODS) FeCrAl alloys are currently under investigation as candidate materials for both fission and fusion reactor applications [3, 4]. These alloys attempt to combine the high temperature oxidation resistance of FeCrAl [4, 5] with the high strength and irradiation resistance of conventional ODS FeCr alloys [1, 6, 7].

One challenge in the development of high-Cr ferritic alloys is that at intermediate temperatures applicable to both fission and fusion reactor applications (300-450°C), Fe-Cr phase separation kinetics favor the precipitation of deleterious Cr-rich α' precipitates within the α-Fe matrix. The precipitation of α'-Cr has been studied for both FeCr [8-11] and FeCrAl [12-14] alloys, with irradiation accelerating α'-α phase separation kinetics [15, 16]. In addition, compositional design regions for FeCrAl alloys have been established to mitigate this phase separation phenomenon after thermal ageing and irradiation [17, 18]. However, few studies have examined the α'-precipitation in ODS variants of FeCr and FeCrAl alloys. A study on a Fe-14Cr ODS alloy MA957 neutron irradiated to 109 dpa at 412°C indicated a high number density ($9x10^{23}$ m^{-3}) of α' precipitates within the matrix [19]. Furthermore, thermal ageing experiments on the legacy ODS (Fe-20Cr-6Al) alloy PM2000 developed by Plansee have indicated α'-α phase separation and the subsequent embrittlement of the alloy [20-22]. The α'-induced embrittlement of these higher Cr (>14 wt.%) ODS FeCr and FeCrAl alloys has led to the development of low-Cr ($\leq$ 12 wt.%) ODS FeCrAl alloys to decrease α'-α phase separation within the material [4].

This work investigates the Cr-rich α' precipitation in a low-Cr (12 wt.%) ODS FeCrAl alloy after neutron irradiation using atom probe tomography, with a specific interest in comparisons with model FeCrAl alloys of similar composition without oxide dispersions. The dependence of α' precipitate stability on irradiation temperature is also discussed. Detailed characterizations of the fine-scale (Y,Al,O) rich precipitate compositions, sizes, and number densities are reported to understand their post-irradiation stability as a function of irradiation temperature.

The ODS FeCrAl alloy investigated in this work, designated 125YF, was produced via the powder metallurgy approach by mechanically alloying Fe-12Cr-5.6Al (wt%) gas atomized powder with nanocrystalline Y_2O_3 followed by degassing at 300°C for 24 h and subsequent extrusion at 950°C. Details concerning the fabrication, microstructure, tensile properties, and oxidation resistance of the as-extruded 125YF alloy are reported elsewhere [3]. Miniature SS-J3 sheet tensile specimens were loaded into rabbit capsules and irradiated in the High Flux Isotope Reactor (HFIR) at Oak Ridge National Laboratory (ORNL) to 1.8 dpa at ~215, 357, and 557°C with corresponding dose rates of $9.3\text{-}9.8x10^{-7}$ dpa/s [23]. The lower temperature irradiations targeted light water reactor operating regimes while the higher temperature irradiation focused on advanced fission/fusion reactor temperature regimes.

Following irradiation, tensile testing was performed on the unirradiated and irradiated 125YF specimens. Details surrounding the mechanical property evaluations of this alloy and subsequent microstructural investigations will be reported in a separate study. One half of the failed tensile specimen for each condition was mounted and polished. Using a focused ion beam (FIB) lift-out technique [24], atom probe tomography (APT) specimens were prepared from the

tensile specimen head using an FEI Quanta 3D dual-beam FIB at ORNL's Low Activation Materials Development and Analysis (LAMDA) Laboratory [25]. APT data collection was performed at the Center for Advanced Energy Studies-Microscopy and Characterization Suite (CAES-MaCS) at Idaho National Laboratory (INL) using a Cameca model 4000X HR Local Electrode Atom Probe (LEAP) with a 36% detection efficiency. The LEAP was operated in laser mode with a pulse frequency of 200 kHz, a laser energy of 32 pJ, and a target detection rate of 0.005 atoms/pulse at 50 K. At least 3 APT specimens were acquired for each condition with at least 8M ions collected per specimen. Cameca's Integrated Visualization and Analysis Software (IVAS) version 3.6.8 was used for both data reconstruction and analysis [26]. The maximum separation method was implemented to identify (Y,Al,O)- and Cr-rich clusters in each control volume [27-29]. Since trajectory aberrations may create local Cr-enrichments in the vicinity of (Y,Al,O)-rich precipitates, the maximum separation was first applied to the (Y,Al,O)-rich precipitates. Following the identification of the (Y,Al,O)-rich nanoprecipitates, the maximum separation method was then applied to the APT specimen in the remaining control volume with (Y,Al,O)-rich precipitates omitted.

Table 1
Comparison of 125YF atom probe tomography specimen bulk compositions (in at.%) as a function of irradiation dose and temperature with previous chemical analysis results [3] using standard peak decompositions.

125YF Specimen	Dose [dpa]	T_{irr}	Fe	Cr	Al	Y	O	C	N
[3]	--	--	78.09	11.79	9.21	0.11	0.63	0.09	0.08
Control (OD34)	--	--	78.00	11.82	9.23	0.06	0.54	0.18	0.01
OD01	1.8	215°C	78.28	11.68	9.24	0.08	0.40	0.11	0.00
OD03	1.8	357°C	77.59	11.65	9.05	0.07	0.33	0.08	0.01
OD06	1.8	557°C	78.49	11.71	9.07	0.09	0.35	0.07	0.00

Table 1 compares the composition of as-fabricated control sample reported elsewhere [3] with the bulk composition of the unirradiated and irradiated specimens calculated using the native peak decomposition algorithm within the IVAS program (reported in at.%). Peak deconvolution is important for accurate compositional corrections for both bulk and precipitate compositions due to the mass-to-charge ratio peak overlap at 27 Da ($^{27}Al^{+1}$, $^{54}Cr^{+2}$, $^{54}Fe^{+2}$). The Y content in all samples is underestimated in comparison to previous chemical analysis results [3], which can partially be explained through the preferential loss in Y content in previous APT studies [30]. However what is more interesting is the drastic underestimation of O content, which has important consequences in compositional accuracy of the (Y,Al,O)-rich precipitates. Standard peak decomposition algorithms in IVAS assume natural isotopic abundances for each element. Although some transmutation reactions may have occurred over the course of the neutron irradiation experiment, it has previously been shown that for model FeCrAl alloys irradiated up to 7 dpa in HFIR, the assumption of natural isotopic abundance results in a negligible compositional error [13]. Since cluster compositions outputted by the maximum separation method are not corrected for peak overlaps, individual cluster compositions for both Cr- and (Y,Al,O)-rich precipitates were corrected using the methodology previously developed by Edmondson et al. for α'-precipitates in neutron irradiated FeCrAl alloys [31].

(Y,Al,O)-rich precipitates were homogeneously distributed throughout the matrix in all samples examined. The average (Y,Al,O) precipitate radii were calculated using the atomic count method assuming spherical equivalent radii [9]. For all conditions, radii were highly consistent and averaged 1.5 $\pm$ 0.6 nm (Table 2). The measured number densities were also high

(4.6-7.4x10^{23} m^{-3}) and comparable to 125Y series ODS FeCrAl alloys previously developed at ORNL (1.4-2.5x10^{23} m^{-3}) [32]. This result indicates that the precipitate sizes and number densities are stable at all irradiation temperatures 215-557°C for the low dose (1.8 dpa) irradiation condition. In addition, the size distributions reported in this work have a dimensional scale comparable to those reported in Zr- and Hf- containing ODS FeCrAl alloys [33, 34], which suggests that it is possible to refine the nanoprecipitate size for enhanced sink strength using optimum processing conditions alone and without the need for significant additional alloying additions beyond the baseline ODS FeCrAl composition.

A previous APT study on neutron irradiated MA957 (109 dpa, 412°C) reported that α' precipitates were anti-correlated with the (Y,Ti,O) nanoprecipitates within the ODS FeCr alloy and preferred to nucleate between precipitates [19]. Thus, to prevent trajectory aberrations from providing false-positive results for Cr-rich clustering behavior around the (Y,Al,O)-rich precipitates, these precipitates were subtracted from the matrix prior to applying the cluster search algorithm on the Cr-rich clusters. Cr-rich clusters were only found in OD03 specimen. The lack of observed α' precipitates in the low temperature OD01 and high temperature OD06 specimens is explained through a consideration of the phase diagram and the irradiation conditions. The higher temperature (557°C) of the OD06 specimen is well above the miscibility gap for α'-α phase separation based on the Fe-Cr phase diagram, so it would be expected that no α' precipitates were noted for any OD06 specimens. Based on the equilibrium phase diagram, α' precipitates should form at the lower OD01 (215°C) temperature. The lack of precipitation could be explained by a competition between the radiation enhanced diffusion of Cr atoms and the ballistic dissolution of these precipitates at this temperature. It is also possible that α'-α phase separation may still occur at 215°C with higher doses (longer ageing times), but future studies are needed to confirm this possibility.

Table 2
Trajectory aberration corrected pre- and post-irradiation precipitate characteristics for each 125YF specimen. Surrounding matrix compositions are also reported. Errors in parenthesis are reported as one standard deviation from the mean. Compositions are in at.%.

Sample	Type	R_p [nm]	N_p x10^{23} [m^{-3}]	Fe	Cr	Al	Y	O
OD34	Matrix	n/a	n/a	78.16 (0.18)	11.83 (0.05)	9.17 (0.12)	0.03 (0.01)	0.46 (0.06)
	Y,Al,O	1.5 (0.6)	4.56 (0.65)	58.26 (10.37)	10.17 (3.58)	13.59 (3.56)	7.70 (7.57)	9.86 (5.00)
OD01	Matrix	n/a	n/a	78.42 (0.29)	11.67 (0.22)	9.23 (0.22)	0.03 (0.01)	0.30 (0.02)
	Y,Al,O	1.5 (0.6)	4.56 (0.31)	59.40 (9.74)	12.75 (3.90)	8.06 (3.27)	8.97 (7.49)	10.11 (4.80)
OD03	Matrix	n/a	n/a	78.54 (0.08)	11.74 (0.16)	9.13 (0.21)	0.02 (0.01)	0.30 (0.02)
	Y,Al,O	1.5 (0.6)	5.47 (0.36)	55.68 (10.68)	11.29 (3.52)	11.66 (3.69)	9.70 (7.89)	10.98 (5.35)
	Cr-rich	1.6 (0.4)	0.78 (0.45)	30.43 (8.35)	60.72 (10.67)	5.37 (2.96)	0.58 (0.69)	2.48 (2.74)
OD06	Matrix	n/a	n/a	78.75 (0.02)	11.70 (0.01)	8.98 (0.01)	0.02 (0.01)	0.25 (0.01)
	Y,Al,O	1.5 (0.6)	7.38 (0.22)	55.63 (12.55)	8.84 (3.32)	13.09 (3.81)	10.96 (9.56)	10.87 (5.99)

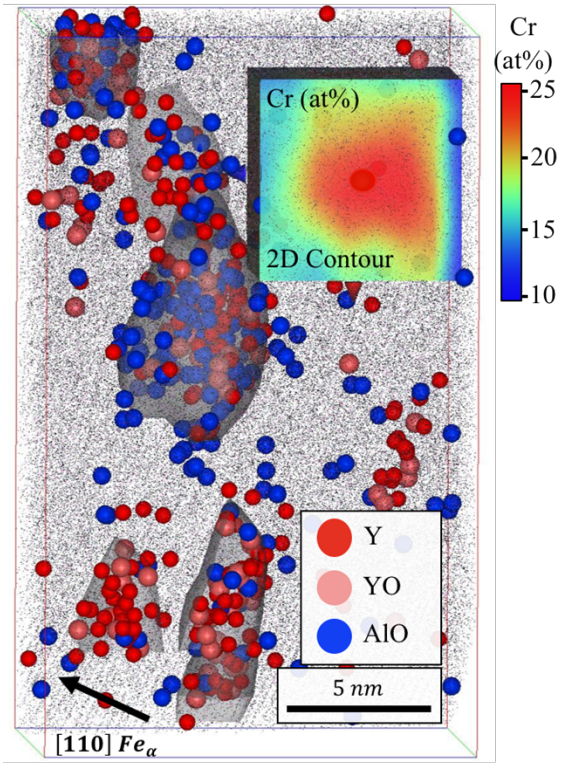

Fig. 1. Y, YO, and AlO atom maps overlaid with black Fe matrix atoms in the OD03 irradiated specimen. Grey 1.5 at% (Y,YO,AlO) isoconcentration surfaces highlight observed nanoprecipitates while an embedded 2D Cr atomic concentration contour plot on a cubic region of interest reveals a Cr-rich precipitate presumed to be α'.

Presented in Fig. 1 is a Cr-rich α' precipitate (illustrated by the embedded 2D contour plot) located near the {110} pole used for the sample reconstruction and nearby (Y,Al,O) precipitates. The Cr concentration shown is for a cubic region of interest (ROI) slightly larger than the precipitate, which includes a substantial contribution from the matrix that shifts the visualized concentration to values lower than the actual cluster composition. The high number density of α' clusters are illustrated in magenta overlaid with the (Y,Al,O) nanoprecipitates in Fig. 2(a). A closer look at one of these selected clusters shows a qualitative enrichment in Cr as illustrated in the Cr-atom map (Fig. 2(b)). A significant increase in the total atomic point density was observed across the precipitates (Fig. 2(c)) which suggests significant trajectory aberrations from the matrix overlapping with the identified precipitates [35, 36]. To correct for matrix contributions to the cluster compositions, the percent increase in point density across the clusters was used to subtract an equivalent fraction of atoms of the matrix composition from the precipitates, resulting in an approximated aberration-corrected cluster composition. Corrections for increased point density variations have previously been applied in a similar manner by Briggs for oxide-free FeCrAl under similar irradiation conditions and temperatures [13]. This aberration-correction methodology was also extended to the population of (Y,Al,O) precipitates in this work.

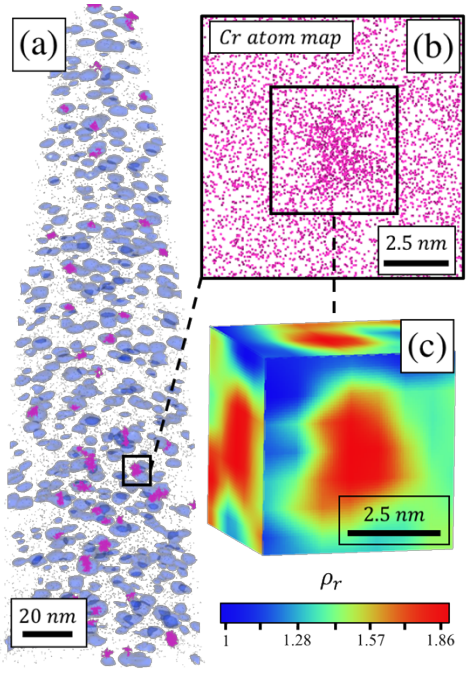

Fig. 2. (a) Reconstructed control volume for OD03 showing blue 1.5 at% (Y,YO,AlO) isoconcentration surfaces for nanoscale precipitates with overlaid magenta Cr-rich precipitates, (b) a Cr atom map for a selected precipitate and (c) 2D density contour plots on the selected control volume. The reduced density (ρ_r) in the 2D contour plot indicates the ratio of atomic density across the precipitate in comparison divided by the lowest atomic point density in the surrounding matrix.

Comparing the measured α' precipitates with model FeCrAl alloys of similar bulk composition shows significant similarities and differences, particularly with respect to cluster composition, size, and number density. Previous APT studies on Fe-12Cr-9Al (at%) neutron irradiated to 7 dpa at a similar temperature (320°C) have reported α' precipitates containing 51-58 at% Cr and 4.5-5 at% Al, in comparison to 61 at% and 5 at% reported in this work [13, 31]. The lower Al content in the clusters supports the conjecture that Al-partitioning has occurred from the α' precipitates to the surrounding matrix previously reported in both model FeCrAl alloys and in thermally aged legacy ODS FeCrAl alloy PM2000 [31, 37]. The reported α' radius in this work is also within the margin of error for the same model FeCrAl alloy (1.6 ± 0.8 nm) [13, 31]. However, the α' precipitate number density reported in this work for the ODS FeCrAl alloy (0.78×10^{23} m^{-3}) is an order of magnitude lower than for the compositionally similar non-ODS model FeCrAl alloy (7×10^{23} m^{-3}), which implies a sink-strength dependency on α' formation [31].

Rate theory approaches simulating the irradiation enhanced α'-α phase separation have indicated that near strong sinks such as grain boundaries the excess concentration of defects is lower and there is a denuded zone absent of precipitates near the boundary [16]. Thus, the precipitate sink strength associated with a high number density of coherent to semi-coherent nanoprecipitates may be sufficient to retard some α' precipitation by locally lowering the defect concentrations near the interfaces. Enriched Cr within the (Y,Al,O) precipitates may also be intrinsic to the precipitate nucleation process, whereby displaced Fe and Cr from the local

precipitate control volume may result in a Cr-rich shell surrounding these precipitates [38-40]. In the present work, the ratio of Cr/Fe within the (Y,Al,O) precipitates is slightly higher than the Cr/Fe ratio of the bulk specimen, but averaged 1D concentration profiles through 50 precipitates indicated no presence of an interfacial shell enriched in Cr (Fig. 3). The total concentration profile length was chosen as 3x the radius of gyration discretized into 100 bins. Although the data presented in this work doesn't support the existence of a Cr-rich shell within the smallest (Y,Al,O) precipitates, there does seem to be a substantial amount of Fe and Cr still within the clusters even after aberration correction. Some authors have compared the Fe and Cr contributions within ODS ferritic alloy nanoprecipitates to what would be expected in small angle neutron scattering experiments and have argued that nearly all of the reported Fe and Cr in the nanoprecipitates are artifacts of the APT technique [36]. Thus, the Fe and Cr contents measured in these precipitates is likely attributed to the imperfect methodology used for compositional correction without knowing the Al-partitioning behavior between the precipitates and the matrix.

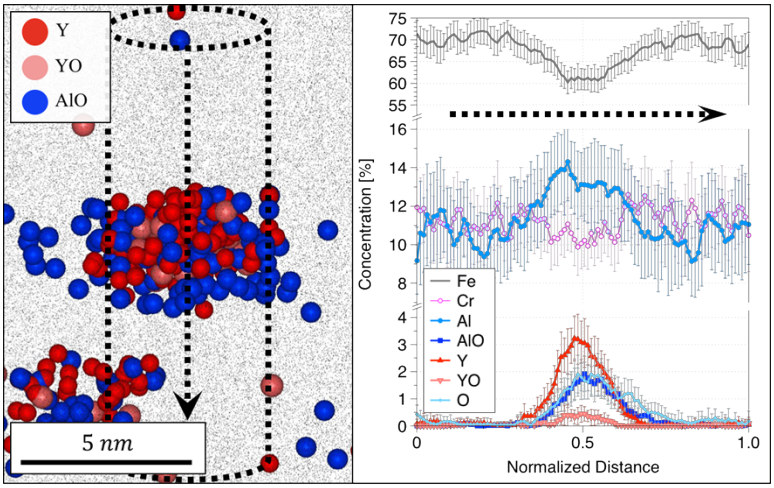

Fig. 3. (a) A representative (Y,Al,O) nano-oxide precipitate showing AlO, YO, and Y atom maps. Black dots indicate the Fe matrix atoms. Also shown are (b) averaged 1D concentration profiles through 50 (Y,Al,O) precipitates within the control volume as a function of normalized distance across the precipitates. Error bars indicate 95% confidence intervals for measured elemental concentrations.

A ternary composition diagram has been generated using 1815 identified nanoprecipitates in the OD03 APT specimens to compare the Y, Al, and O ratios in comparison to expected stochiometric compositions (**Fig. 4(a)**). Discretizing the ternary diagram into 50 bins, the number of clusters in each bin was quantified and a frequency hit map was generated describing the probability of finding clusters in representative compositional regions. Clusters appear to be generally non-stochiometric with a broad range of compositions. Smaller clusters are less rich in Al, while the average Y/Al ratio tends to favor what would be expected for the YAG ($Y_3Al_5O_{12}$) composition. The unirradiated (OD34) and irradiated specimens (OD01, OD06) exhibited the same compositional spread. In all specimens, the O content is highly underestimated, which is explained through the larger spatial distribution in O atoms [41] and other APT artifacts [42]. This is supported by the substantial fraction of O remaining in the matrix after subtracting the

identified (Y,Al,O) precipitates (Table 2). It has also been shown that uncalibrated laser parameters results in differences in measured O content in materials studied in laser-mode [43].

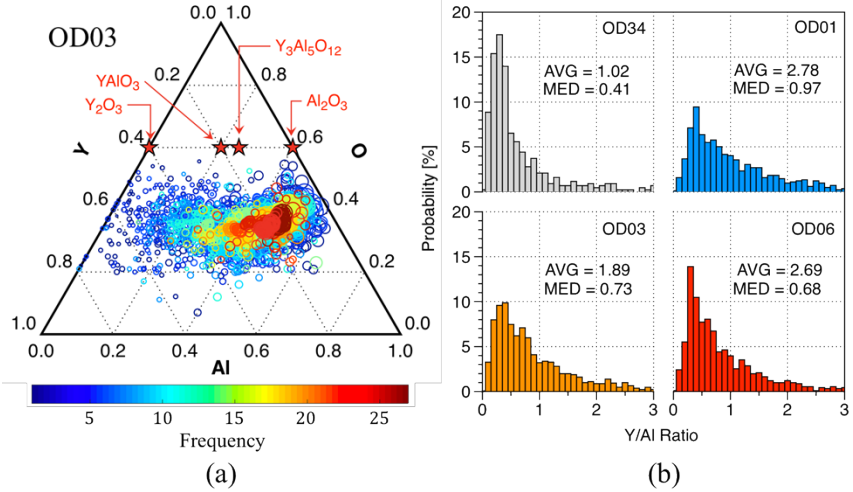

Fig. 4. (a) the Ternary Y-Al-O diagram comparing nano-oxide compositions with expected stochiometric phases for specimen OD03. Point diameters are proportional to nano-oxide diameters, while colors are mapped using the displayed hit map frequency distribution. Also shown is the (b) distribution of Y/Al ratio for unirradiated 125YF alloy OD34 in comparison to samples irradiated to 1.8 dpa at 215°C (OD01), 357°C (OD03), and 557°C (OD06).

Although there exist similar compositional spreads for all (Y,Al,O)-rich precipitates, there does seem to be an effect of irradiation on the compositions of these precipitates. Consider the distribution of Y/Al ratios presented in **Fig. 4(b)**. Before irradiation, the median Y/Al ratio is 0.41, which is similar to what would be expected for the YAG phase (0.6). After irradiation, the Y/Al ratio increases, but the increase in this ratio decreases with increasing temperature. This suggests that at lower temperatures where ballistic dissolution dominates, a greater change in precipitate composition exists, while at higher temperatures where atoms are more able to back-diffuse to the precipitates, the Y/Al ratio tends to drive toward the initial precipitate composition.

An examination of the atom probe tomography results presented in this work suggests that the (Y,Al,O) nanoprecipitate sizes within this ODS FeCrAl alloy are stable under neutron irradiation to a dose of 1.8 dpa at temperatures relevant to both current and advanced reactor concept temperature regimes. This is supported by the consistency of the sizes and number densities for these precipitates in comparison to the control sample across the irradiation condition studied. However, there may be an effect of irradiation temperature on the compositions of these precipitates as ballistic dissolution and back-diffusion of solute atoms compete. In the sample irradiated at 357°C, α'-α phase separation was noted and quantified, with compositions and sizes similar to those previously investigated in neutron irradiated non-ODS FeCrAl alloys of similar composition. A significant finding is that the number density of α'-precipitates is lower by about an order of magnitude in 125YF than in model FeCrAl after irradiation at 357°C.

Acknowledgments

Primary characterization efforts were funded by a Nuclear Science User Facilities Rapid Turnaround Experiment (17-961) and was conducted at the Center for Advanced Energy Studies-Microscopy and Characterization Suite (CAES-MaCS). A portion of the irradiation campaign, including capsule design, capsule opening, radioactive specimen handling/preperation, and data analysis, was sponsored by the DOE-NE, Advanced Fuel Campaign of the Nuclear Technology Research and Development programs. Neutron irradiation of the 125YF specimens at ORNL's HFIR user facility was sponsored by the Scientific User Facilities Division, Office of Basic Energy Sciences, DOE. The authors would like to thank Jatuporn Burns and Dr. Yaqiao Wu for their assistance with instrument operation at the MaCS facility and the Irradiated Materials Examination and Testing facility and LAMDA laboratory staff for their continuing support of this research. This material is based upon work supported under a Department of Energy Nuclear Energy University Programs (NEUP) Graduate Fellowship.

References

[1] S.J. Zinkle, L.L. Snead, Annual Review of Materials Research 44(1) (2014) 241-267.
[2] B.A. Pint, K.A. Terrani, M.P. Brady, T. Cheng, J.R. Keiser, Journal of Nuclear Materials 440(1-3) (2013) 420-427.
[3] S. Dryepondt, K.A. Unocic, D.T. Hoelzer, C.P. Massey, B.A. Pint, Journal of Nuclear Materials 501 (2018) 59-71.
[4] B.A. Pint, S. Dryepondt, K.A. Unocic, D.T. Hoelzer, JOM 66(12) (2014) 2458-2466.
[5] K.A. Terrani, S.J. Zinkle, L.L. Snead, Journal of Nuclear Materials 448(1-3) (2014) 420-435.
[6] S.J. Zinkle, J.L. Boutard, D.T. Hoelzer, A. Kimura, R. Lindau, G.R. Odette, M. Rieth, L. Tan, H. Tanigawa, Nuclear Fusion 57(9) (2017) 092005.
[7] G.R. Odette, Scripta Materialia 143 (2018) 142-148.
[8] F. Bley, Acta metallurgica et materialia 40(7) (1992) 1505-1517.
[9] M. Bachhav, G. Robert Odette, E.A. Marquis, Scripta Materialia 74 (2014) 48-51.
[10] D. Chen, A. Kimura, W. Han, Journal of Nuclear Materials 455(1-3) (2014) 436-439.
[11] E.R. Reese, M. Bachhav, P. Wells, T. Yamamoto, G. Robert Odette, E.A. Marquis, Journal of Nuclear Materials 500 (2018) 192-198.
[12] K.G. Field, X. Hu, K.C. Littrell, Y. Yamamoto, L.L. Snead, Journal of Nuclear Materials 465 (2015) 746-755.
[13] S.A. Briggs, P.D. Edmondson, K.C. Littrell, Y. Yamamoto, R.H. Howard, C.R. Daily, K.A. Terrani, K. Sridharan, K.G. Field, Acta Materialia 129 (2017) 217-228.
[14] K.G. Field, K.C. Littrell, S.A. Briggs, Scripta Materialia 142 (2018) 41-45.
[15] M.H. Mathon, Y. de Carlan, G. Geoffroy, X. Averty, A. Alamo, C.H. de Novion, Journal of Nuclear Materials 312(2-3) (2003) 236-248.
[16] F. Soisson, T. Jourdan, Acta Materialia 103 (2016) 870-881.
[17] S. Kobayashi, T. Takasugi, Scripta Materialia 63(11) (2010) 1104-1107.
[18] J. Ejenstam, M. Thuvander, P. Olsson, F. Rave, P. Szakalos, Journal of Nuclear Materials 457 (2015) 291-297.
[19] N.A. Bailey, E. Stergar, M. Toloczko, P. Hosemann, Journal of Nuclear Materials 459 (2015) 225-234.
[20] C. Capdevila, M.K. Miller, K.F. Russell, J. Chao, J.L. González-Carrasco, Materials Science and Engineering: A 490(1-2) (2008) 277-288.

[21] C. Capdevila, M.K. Miller, J. Chao, Acta Materialia 60(12) (2012) 4673-4684.
[22] Z. Száraz, G. Török, V. Kršjak, P. Hähner, Journal of Nuclear Materials 435(1-3) (2013) 56-62.
[23] M.N. Gussev, E. Cakmak, K.G. Field, Journal of Nuclear Materials 504 (2018) 221-233.
[24] M.K. Miller, K.F. Russell, Ultramicroscopy 107(9) (2007) 761-766.
[25] C.M. Parish, N.K. Kumar, L.L. Snead, P.D. Edmondson, K.G. Field, C. Silva, A.M. Williams, K. Linton, K.J. Leonard, Microscopy and Microanalysis 21(S3) (2015) 1003-1004.
[26] B. Gault, M.P. Moody, J.M. Cairney, S.P. Ringer, Atom probe microscopy, Springer, 2012.
[27] E.A. Marquis, J.M. Hyde, Materials Science and Engineering: R: Reports 69(4-5) (2010) 37-62.
[28] L.T. Stephenson, M.P. Moody, P.V. Liddicoat, S.P. Ringer, Microscopy and Microanalysis 13(6) (2007) 448-463.
[29] D. Vaumousse, A. Cerezo, P. Warren, Ultramicroscopy 95 (2003) 215-221.
[30] C.A. Williams, G.D. Smith, E.A. Marquis, Ultramicroscopy 125 (2013) 10-7.
[31] P.D. Edmondson, S.A. Briggs, Y.Yamamoto, R.H. Howard, K. Sridharan, K.A. Terrani, K.G. Field, Scripta Materialia 116 (2016) 112-116.
[32] K.A. Unocic, B.A. Pint, D.T. Hoelzer, Journal of materials science 51(20) (2016) 9190-9206.
[33] P. Dou, A. Kimura, R. Kasada, T. Okuda, M. Inoue, S. Ukai, S. Ohnuki, T. Fujisawa, F. Abe, Journal of Nuclear Materials 444(1-3) (2014) 441-453.
[34] P. Dou, A. Kimura, R. Kasada, T. Okuda, M. Inoue, S. Ukai, S. Ohnuki, T. Fujisawa, F. Abe, S. Jiang, Z. Yang, Journal of Nuclear Materials 485 (2017) 189-201.
[35] D. Blavette, F. Vurpillot, P. Pareige, A. Menand, Ultramicroscopy 89(1-3) (2001) 145-153.
[36] C. Hatzoglou, B. Radiguet, P. Pareige, Journal of Nuclear Materials 492 (2017) 279-291.
[37] C. Capdevila, M.K. Miller, K.F. Russell, Journal of Materials Science 43(11) (2008) 3889-3893.
[38] E.A. Marquis, Applied Physics Letters 93(18) (2008).
[39] L.L. Hsiung, M.J. Fluss, A. Kimura, Materials Letters 64(16) (2010) 1782-1785.
[40] L.L. Hsiung, M.J. Fluss, S.J. Tumey, B.W. Choi, Y. Serruys, F. Willaime, A. Kimura, Physical Review B 82(18) (2010) 184103.
[41] C.A. Williams, E.A. Marquis, A. Cerezo, G.D.W. Smith, Journal of Nuclear Materials 400(1) (2010) 37-45.
[42] B. Gault, D.W. Saxey, M.W. Ashton, S.B. Sinnott, A.N. Chiaramonti, M.P. Moody, D.K. Schreiber, New Journal of Physics 18(3) (2016).
[43] S. Pedrazzini, A.J. London, B. Gault, D. Saxey, S. Speller, C.R.M. Grovenor, M. Danaie, M.P. Moody, P.D. Edmondson, P.A.J. Bagot, Microsc Microanal 23(2) (2017) 414-424.